catalysts

MDPI

Article

Design of Unsupported Ni–Ba Catalysts for the CO_2 Storage-Regeneration (CO_2-SR) Process: Role of Ni/Ba Surface Domains and Rh Promotion

Sofía Essounani-Mérida [1,2], Sergio Molina-Ramírez [1], Marina Cortés-Reyes [1,2], Concepción Herrera [1,2,*], Elisabetta Finocchio [3], María Ángeles Larrubia [1,*] and Luis J. Alemany [1]

[1] Departamento de Ingeniería Química, Facultad de Ciencias, Campus de Teatinos, Universidad de Málaga, 29071 Malaga, Spain; sofiaess@uma.es (S.E.-M.); smolina@uma.es (S.M.-R.); marinacr@uma.es (M.C.-R.); luijo@uma.es (L.J.A.)
[2] Instituto Universitario de Materiales y Nanotecnología, IMANA, Campus de Teatinos, Universidad de Málaga, 29071 Malaga, Spain
[3] Dipartimento di Ingegneria Civile, Chimica e Ambientale, Università di Genova, 16145 Genova, Italy; elisabetta.finocchio@unige.it
* Correspondence: concepcionhd@uma.es (C.H.); mavargas@uma.es (M.Á.L.)

Abstract

The CO_2 storage–regeneration (CO_2-SR) process represents a promising strategy for integrating CO_2 capture and catalytic conversion within a single cyclic operation using multifunctional catalysts. In this concept, CO_2 is first stored on basic sites and subsequently converted through methane activation, enabling the coupling of CO_2 capture and reforming reactions in a single reactor. In this work, a series of unsupported Ni–Ba catalysts were investigated as model multifunctional materials for the CO_2-SR process. Catalysts with different Ni/Ba ratios were prepared to analyze how the distribution of storage and catalytic sites influences the cyclic CO_2 capture–conversion behavior. In addition, Rh was introduced as a promoter either during synthesis by co-precipitation or ex situ by impregnation, allowing to evaluate the influence of Rh location and surface enrichment on the catalytic properties. Rh incorporation in the NiBa catalyst (Ni/Ba = 10/1 and Ni/Rh = 100/1) increased the specific surface area (BET area 64 $m^2 \cdot g^{-1}$ vs. 55 $m^2 \cdot g^{-1}$ for NiBa) and reduced the NiO crystallite size from 250.4 Å to 231.5 Å, indicating improved dispersion of the metallic phase. XPS analysis revealed the coexistence of Rh^0 and Rh^{3+} species, suggesting that Rh acts as a redox mediator that facilitates hydrogen activation and promotes hydrogen spillover to neighboring Ni sites. Raman and CO_2-TPD results show that Ba-derived domains stabilize carbonate species responsible for CO_2 storage, while Rh enhances catalyst reducibility and modifies the kinetics of carbonate decomposition during the regeneration stage. Transient CO_2–CH_4 pulse experiments demonstrate that the CO_2-SR process proceeds through a dynamic surface cycle involving reversible carbonate formation on Ba-derived basic sites coupled with methane activation on Ni-containing interfacial sites. The results indicate that catalyst performance is governed by a hierarchical surface architecture composed of Ni–O–Ba interfacial domains, reversible Ba–O–Ba carbonate storage sites, and more stable Ba-rich domains. The distribution of these domains, controlled by the Ni/Ba ratio and the dispersion of the metallic phase, determines the reversibility of carbonate formation and the efficiency of the cyclic CO_2 storage–regeneration process.

Keywords: CO_2 storage–regeneration (CO_2-SR); Ni–Ba catalysts; surface domains; CO_2 capture and conversion; Rh promotion; cyclic CO_2–CH_4 operation

Check for updates

Academic Editor: María Atienza-Martínez

Received: 6 March 2026
Revised: 13 April 2026
Accepted: 18 April 2026
Published: 23 April 2026

Copyright: © 2026 by the authors. Licensee MDPI, Basel, Switzerland. This article is an open access article distributed under the terms and conditions of the Creative Commons Attribution (CC BY) license.

1. Introduction

The mitigation of anthropogenic carbon dioxide (CO_2) emissions remains one of the most pressing challenges in the transition toward sustainable energy systems. Among the proposed solutions, catalytic strategies that integrate CO_2 capture with its direct conversion into value-added products have attracted increasing attention. In particular, the so-called CO_2 Capture, Storage and Utilization process has emerged as a cost-effective alternative to conventional capture and utilization schemes [1–3]. This approach relies on the periodic adsorption and subsequent conversion of CO_2 using Dual Function Materials (DFMs).

Currently, two main technical routes are employed for in situ CO_2 conversion to syngas: dry reforming of methane (DRM) [4–8] and the reverse water–gas shift (RWGS) reaction [9–11]. Syngas production is a key intermediate for numerous downstream chemical processes. Unlike traditional CO_2 capture and utilization strategies, this integrated approach shortens the CO_2 utilization pathway by eliminating intermediate separation, purification, and transportation steps. Conventionally, the process is implemented in two independent reactors: (1) CO_2 capture from flue gas in an adsorption reactor, followed by (2) conversion of the stored CO_2 in a second reactor.

Alkali and alkaline-earth metals, together with their oxides, hydroxides, and salts, play a central role in CO_2 capture due to their strong basicity and high affinity for acidic molecules such as CO_2. These materials readily interact with CO_2, forming carbonates and bicarbonates through chemisorption processes. Their crystalline structures allow reversible CO_2 incorporation and release [12], a critical feature given the low intrinsic reactivity and weak polarity of the CO_2 molecule. Through acid–base interactions, these solids provide an effective environment for CO_2 activation. Among them, calcium and magnesium oxides and hydroxides are widely regarded as benchmark materials for solid CO_2 capture [13]. Calcium oxide reacts readily with CO_2 to form calcium carbonate, which can be thermally decomposed to regenerate CaO, making it a model system for cyclic sorption processes. Once captured, CO_2 can be converted into valuable products such as synthetic fuels or methanol. Combining basic sites from alkali or alkaline-earth metal oxides/hydroxides with transition metals (e.g., Ni or Cu) yields multifunctional catalysts capable of promoting hydrogenation reactions toward methane, methanol, or light hydrocarbons via syngas intermediates.

Within this framework, we have recently developed the so-called CO_2-SR (storage and regeneration) technology, a cyclic process analogous to Lean NO_x Trap (LNT-NO_x) systems. In this approach, CO_2 is captured from flue gas streams and subsequently converted in situ into syngas via reforming with methane, using a single hybrid catalyst in a single reactor. The integration of capture and conversion within one reactor, combined with the use of a homogeneous hybrid material, offers significant advantages in terms of process intensification. These bifunctional catalysts incorporate alkaline or alkaline-earth metals as labile CO_2 storage components (CO_2 storage) and Ni as the active phase for the reforming reaction, enabling continuous catalyst regeneration (CO_2 regeneration) under cyclic operation and yielding a hydrogen-enriched syngas stream [14,15]. The nature of the alkaline or alkaline-earth metal strongly influences both the textural and electronic properties of the catalyst, thereby affecting CO_2 storage capacity and regeneration efficiency during CH_4 conversion.

In particular, the metal–Ba system exhibits substantial oxygen-storage capacity and a rapid response to redox conditions. The presence of Ba^{2+} confers a bifunctional character, combining a hydroxyl-rich basic surface with a highly adaptable oxygen reservoir. This synergy enables reversible CO_2 chemisorption and efficient oxygen exchange during cyclic operation at moderate temperatures. Throughout repeated storage–regeneration cycles, the catalyst surface remains actively involved in redox processes, facilitating the oxidation of residual species and the restoration of active sites [15].

Nickel-based catalysts have been extensively studied for CO_2 reforming because of their high activity and significantly lower cost relative to noble metals. Nickel remains the industrial standard for methane reforming, including steam reforming and DRM, owing to its strong methane activation capability and economic viability. However, conventional Ni catalysts often suffer from limited stability, sintering, and poor selectivity under harsh conditions. Metallic Ni sites readily dissociate methane into CH_x intermediates and surface carbon, leading to catalyst deactivation [16].

The use of promoters such as alkali and alkaline-earth metals has been shown to markedly modify the physicochemical properties of Ni catalysts. These promoters enhance surface basicity, improve catalytic activity and stability, and can function as an "oxygen reservoir" that facilitates the removal of surface carbon via gasification or controlled oxidation [15–17]. Increased basicity also enhances CO_2 adsorption and alters the electronic environment of Ni active sites, thereby suppressing carbon formation pathways such as the Boudouard reaction [18]. Notably, Ba-containing Ni catalysts have demonstrated to improve CO_2 conversion in the RWGS reaction, highlighting the role of barium in stabilizing carbonate species and enabling efficient redox cycling.

Similarly, the incorporation of small amounts of noble metals—particularly Rh—into Ni catalysts to form Ni–Rh bimetallic systems introduce strong synergistic effects. These include enhanced reducibility, improved metal dispersion, greater resistance to sintering and coke formation, and overall superior catalytic performance. Rh promotes hydrogen spillover, lowering the reduction temperature of Ni and facilitating the formation of active metallic Ni sites under mild conditions [19]. Ni–Rh systems lead to modifications in the electronic and geometric properties of the active phase, influencing adsorption energies of CH_4, CO_2, and reaction intermediates, as well as reaction pathways. Recent low-temperature DRM studies (400–600 °C) have shown that Ni–Rh/γ-Al_2O_3 catalysts outperform monometallic Ni, exhibiting higher conversions and reduced deactivation rates [20]. The presence of Rh also suppresses coke formation, likely through enhanced carbon oxidation and altered nucleation kinetics, while helping to maintain small Ni particle sizes and prevent sintering under thermal stress [21]. Consequently, Ni–Rh catalysts demonstrate improved long-term stability, particularly at lower operating temperatures [20].

From a broader perspective, the use of Rh as a promoter in Ni-based reforming catalysts addresses key limitations of Ni, including carbon accumulation, thermal sintering, and poor durability. By combining Ni's affordability with Rh's noble-metal attributes, such as improved reducibility, resistance to deactivation, and modified surface chemistry, Ni–Rh bimetallic systems offer a compelling balance between cost and performance. These catalysts have therefore emerged as some of the most promising and economically attractive formulations for next-generation methane-reforming technologies, particularly for DRM and sustainable syngas production.

Advanced spectroscopic and temperature-programmed techniques, including FT-IR, Raman, XPS, and TPR, are essential tools for elucidating promoter-induced structural and electronic modifications and for monitoring the evolution of surface species during CO_2 adsorption and reduction. These techniques provide critical insight into the interactions among Ni, Ba, and Rh species, the formation of carbonate intermediates, and the redox behavior of catalysts under realistic operating conditions. Despite these advances, the behavior of unsupported Ni-based bimetallic catalysts under cyclic CO_2–CH_4 environments remains insufficiently understood.

In this work, we investigate the morphological, structural, and redox properties of unsupported NiBa and NiBaRh catalysts, focusing on their CO_2 storage–regeneration performance and surface transformations. By combining advanced FT-IR characterization techniques with cyclic CO_2–CH_4 experiments, we aim to elucidate the roles of Ba and Rh

promoters in modulating Ni-based catalytic systems and to contribute to the rational design of efficient and robust catalysts for CO_2 utilization.

2. Results and Discussion

The morphological and structural properties of the unsupported NiBa 10/1 and NiBaRh 10/2/0.1 catalysts are summarized in Table 1. Both materials exhibit relatively high surface areas, with NiBaRh presenting a slightly higher value (64 $m^2 \cdot g^{-1}$) than NiBa (55 $m^2 \cdot g^{-1}$). The pore volume remains similar for both catalysts (0.09–0.10 $cm^3 \cdot g^{-1}$), while the average pore diameter decreases from 75.2 Å for NiBa to 57.3 Å for NiBaRh, indicating a more compact porous structure upon Rh incorporation. Table 1 shows the atomic ratios calculated using the relative areas of the Ni2p, Rh3d, and Ba4d bands, demonstrating a good correlation with the theoretical metal amounts used in catalyst preparation for Ni and Ba content. Additionally, these atomic ratios were also calculated using ICP, revealing only slight differences. Thus, the Ni/Ba ratio varies from 9 to 9.5 in the NiBaRh (10/1/0.1) catalyst and from 5.1 to 4.6 in the NiBaRh (10/2/0.1) catalyst, calculated from ICP and from XPS, respectively. However, the amount of Rh is significantly lower in the ICP analysis, being close to that used in system preparation.

Table 1. Morphological and structural properties of the NiBa 10/1 and NiBaRh 10/2/0.1 catalysts, including Ni/Rh and Ni/Ba surface ratios obtained from XPS.

	A_{BET} [a] $m^2 \cdot g^{-1}$	V_p [b] $cm^3 \cdot g^{-1}$	d_p [c] Å	NiO Crystal Size [d] Å	Ni/Ba [e] -	Ni/Rh [e] -
NiBa 10/1	55	0.10	75.2	250.4	9.5/1	-
NiBaRh 10/2/0.1	64	0.09	57.3	231.5	4.6/1	93.6/1

[a] calculated by BET equation, [b] BET adsorption pore volume, [c] BET adsorption average pore diameter (4V/A), [d] average crystalline diameter using Rietveld refinement from XRD, and [e] from XPS measurements.

Figure 1 shows the X-ray diffraction patterns of the unsupported NiBa and NiBaRh catalysts after calcination at 800 °C and after reduction in 3% H_2 at 600 °C for 1 h. For the calcined samples, sharp diffraction peaks located at 37.76°, 43.76°, 63.4°, and 75.6° are observed, which correspond to the reflections of face-centered cubic NiO (ICDD no. 04-016-1090). In addition, diffraction peaks assigned to crystalline $BaCO_3$ (ICDD no. 04-016-3101) are detected in both catalysts, indicating that part of the barium species remains as carbonate even after high-temperature calcination. The incorporation of Rh does not lead to the formation of additional crystalline phases detectable by XRD, suggesting that Rh is either highly dispersed or present in amounts below the detection limit of the technique. After reduction under hydrogen, the diffraction peaks corresponding to NiO decrease significantly in intensity and new reflections appear at 44.5°, 51.86°, and 76.39°, which are characteristic of metallic Ni with a cubic crystal structure (ICDD no. 04-006-1675). This transformation confirms the reduction of NiO to metallic Ni under the applied activation conditions. Similar behavior has been previously reported for Ni-based DFMs [15]. The relative intensity of the metallic Ni reflections appears slightly modified in the NiBaRh catalyst compared with NiBa, suggesting that Rh incorporation influences the reduction process and facilitates the dispersion of the metallic phase.

Additionally, the NiO crystallite size estimated from the XRD patterns of calcined samples shows a slight decrease when Rh is present. The NiBaRh catalyst exhibits a crystallite size of 231.5 Å compared to 250.4 Å for NiBa. This reduction suggests that Rh incorporation affects the nucleation or growth of NiO domains during synthesis, leading to improved dispersion of Ni species.

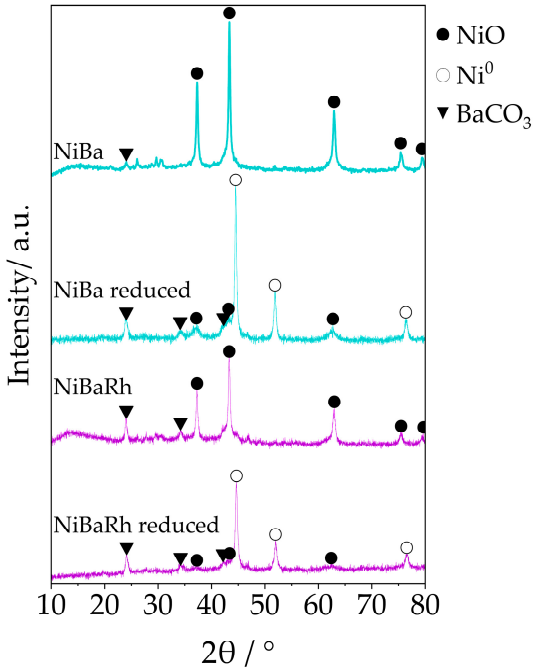


Figure 1. XRD patterns of NiBa 10/1 and NiBaRh 10/2/0.1 catalysts after calcination at 800 °C and after reduction in 3% H_2 at 600 °C for 1 h.

Although Rh-related phases are not detected, likely due to their low concentration or high dispersion, the structural evolution observed after reduction suggests that Rh incorporation may facilitate the transformation of NiO into metallic Ni.

The Raman spectra of the NiBa and NiBaRh catalysts after calcination and after reduction treatment are presented in Figure 2. For the calcined NiBa catalyst, the Raman spectrum shows a dominant band at approximately 505 cm^{-1}, which can be attributed to the Ni–O stretching vibration characteristic of NiO. A weak and broad feature extending toward higher wavenumbers around 700–800 cm^{-1} is also observed, which may be associated with lattice distortions or defect-related modes in the NiO structure. In contrast, the Raman spectrum of the NiBaRh catalyst in the calcined form shows additional bands close at 791 and 1094 cm^{-1}, which can be assigned to vibrational modes of carbonate species associated with $BaCO_3$ [22]. The presence of these bands indicates that carbonate structures are more clearly detectable in the Rh-containing catalyst, in agreement with the coexistence of NiO and Ba-derived carbonate phases also identified by XRD according to a lower Ni/Ba ratio (10/2).

After reduction under hydrogen at 600 °C, the Raman spectra of both catalysts become essentially featureless, with the disappearance of the NiO-related band at ~505 cm^{-1}. This behavior is consistent with the transformation of NiO into metallic Ni, which is Raman-inactive due to its metallic nature and face-centered cubic structure [23]. However, weak contributions associated with carbonate species remain detectable in the reduced samples, indicating that Ba-derived carbonate structures persist. The Raman results support the structural information obtained from XRD, confirming the coexistence of NiO and Ba-containing carbonate phases in the calcined catalysts and the transformation of NiO into metallic Ni after reduction.

Additional insight into the structural differences between the catalysts is provided by the H_2-TPR experiments, which reveal significant variations in the reducibility of the Ni-containing phases depending on both the Ni/Ba ratio and the presence of Rh. In general, the reduction of Ni^{2+} to metallic Ni^0 is often described in the literature [24] as a single-step process corresponding to the reaction $NiO + H_2 \rightarrow Ni^0 + H_2O$. However, in practice, the reduction profile frequently appears broadened or split into multiple features

due to differences in the local environment of Ni species, such as variations in crystallite size, metal–oxide interactions or the presence of interfacial species. Deconvolution of the TPR profiles (Figure 3) reveals two main reduction features close at 590 and 700 °C for the NiBaRh catalyst and 642 and 737 °C for the NiBa catalyst, corresponding to the reduction of two distinct Ni populations. The relative areas of the fitted peaks indicate that, in the NiBa catalyst, the high-temperature contribution accounts for roughly 60–65% of the total hydrogen consumption, while the lower-temperature peak represents about 35–40%. In contrast, the Rh-promoted catalyst exhibits a larger fraction of the low-temperature reduction feature (≈55–60%), indicating an increased population of more easily reducible Ni species associated with Ni–O–Ba interfacial environments. The presence of Rh clearly promotes the reduction of the Ni-containing phases, as evidenced by the systematic shift of both reduction peaks toward lower temperatures. This behavior is commonly attributed to the ability of Rh to activate molecular hydrogen and promote hydrogen spillover, facilitating hydrogen transfer to neighboring Ni species. The combined TPR and deconvolution results therefore indicate that the reducibility of the catalyst is strongly governed by the distribution of Ni environments and by the formation of Ni–O–Ba interfacial sites, which play a key role in the redox of the system during the cyclic CO_2-SR process.

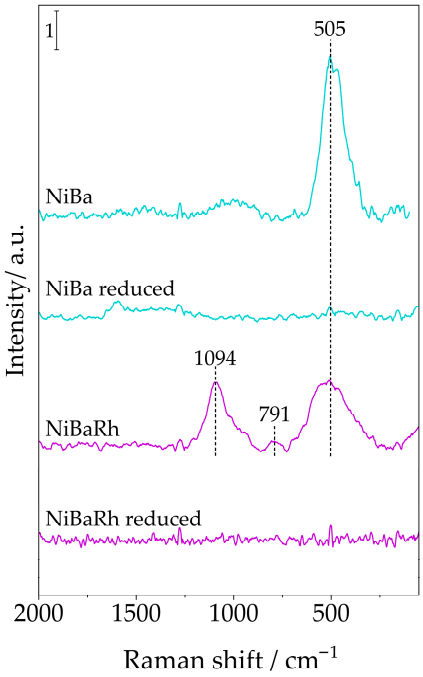


Figure 2. Raman spectra of NiBa 10/1 and NiBaRh 10/2/0.1 catalysts after calcination and after reduction treatment in 3% H_2 at 600 °C for 1 h.

In the catalysts, the TPR profiles (Figure 3) clearly exhibit two distinguishable hydrogen consumption features, indicating that Ni^{2+} species exist in at least two different structural environments. The lower-temperature signal can be associated with the reduction of more weakly interacting Ni species or Ni sites located at dynamic Ni–O–Ba interfaces, which are more accessible to hydrogen and therefore reduced at lower temperatures. In contrast, the higher-temperature peak likely corresponds to Ni^{2+} species (Ni–O–Ni) associated with Ni species close to Ba-containing domains. Thus, the presence of two reduction features should not be interpreted as evidence of different reduction pathways for Ni^{2+} itself, but rather because of heterogeneity in the structural environment surrounding the Ni species.

Further insight into the surface composition and chemical environment of the catalysts is obtained from the XPS analysis, which reveals important differences in the oxidation states of the metallic species and in the distribution of surface oxygen species. The Ni

$2p_{3/2}$ spectra indicate that nickel is predominantly present as Ni^{2+} in the calcined catalysts, consistent with the presence of NiO or Ni species interacting with Ba-containing phases. For the NiBa catalyst, the Ni $2p_{3/2}$ region exhibits a main peak centered at 855.1 eV accompanied by a satellite feature at 861.1 eV, which are characteristic of Ni^{2+} species in NiO [25]. The Ba $4d_{5/2}$ region shows signals located at 87.9 eV and 89.9 eV, which can be attributed to BaO and carbonate-related species [26]. The presence of these species reflects the ability of barium to interact with CO_2 and stabilize carbonate-type surface structures, in agreement with the Raman and XRD results (Table 2).

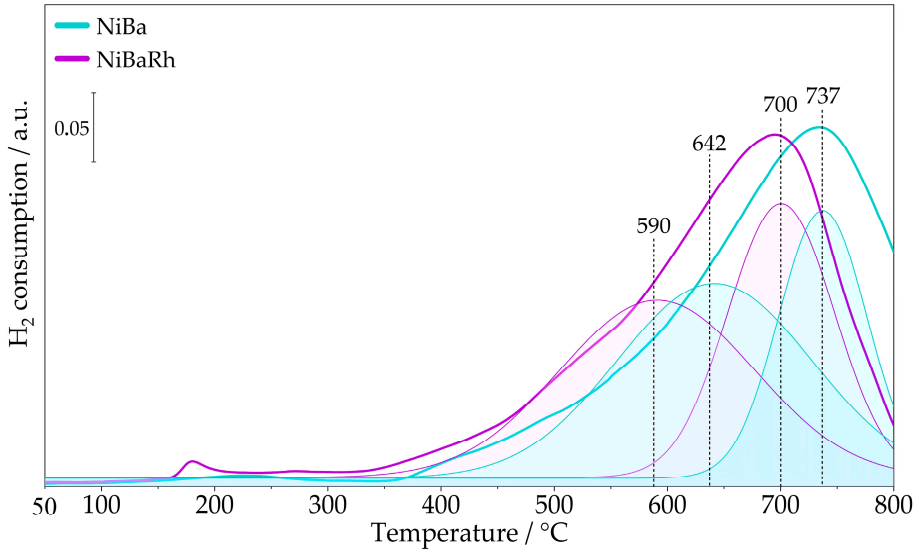


Figure 3. H_2-TPR profiles of the calcined unsupported NiBa 10/1 and NiBaRh 10/2/0.1 catalysts.

Table 2. XPS data summary of calcined samples at 800 °C. Binding energy (eV) after band deconvolution and species identification.

Catalyst	Ni $2p_{3/2}$		Ba $4d_{5/2}$		Rh $3d_{5/2}$	
	B. E. (eV)	Species	B. E. (eV)	Species	B. E. (eV)	Species
NiBa 10/1	855.1	Ni^{+2}	87.9	BaO	-	-
	861.1	Ni^{+2} sat.	89.9	$BaO.CO_2$ $BaO.NiO$	-	-
NiBaRh 10/2/0.1	854.2	Ni^{+2}	89.8	BaO	306.6	Rh^0
	860.2	Ni^{+2} sat.	92.8	$BaO.CO_2$ $BaO.NiO$	308.9	Rh^{3+}

Additionally, the Rh $3d_{5/2}$ spectra show that rhodium is present as a mixture of metallic Rh^0 (306.6 eV) and oxidized Rh^{3+} species (308.9 eV) already in the calcined materials. Quantitative analysis indicates that approximately 35.7% of Rh is present as Rh^0 and 64.3% as Rh^{3+} [27]. The presence of partially reduced Rh under these conditions indicates that rhodium exhibits a significantly higher reducibility than Ni, and that a fraction of the Rh species can exist in the metallic state even before the reduction treatment. This finding aligns with the well-known tendency of Rh to form metallic particles more readily than Ni and suggests that Rh may act as an efficient site for hydrogen activation, facilitating subsequent reduction processes in nearby Ni-sites.

The Ni $2p_{3/2}$ peak in the NiBaRh 10/2/0.1 catalyst appears at a slightly lower binding energy (854.2 eV) compared with NiBa, suggesting a modification of the electronic environment of Ni in the presence of Rh. Meanwhile, the Ba $4d_{5/2}$ signals remain associated with oxide and carbonate species, although small shifts in binding energy are observed, indicating changes in the local chemical environment induced by the incorporation of Rh.

Additional information about the surface oxygen environment is obtained from the O 1s core-level spectra (Figure 4). Deconvolution of the spectra reveals three main contributions associated with different oxygen environments [28]. The first component (O_I, 529.5–530.0 eV) corresponds to lattice oxygen associated with metal–oxygen bonds such as Ni–O or Ba–O. The second component (O_{II}, 531.4–531.9 eV) is attributed to defective or interfacial oxygen species, including hydroxyl groups, chemisorbed oxygen and oxygen associated with structural defects at the metal–oxide interface [29]. The third component (O_{III}, ~532.8–533.0 eV) is assigned to weakly bound oxygen species such as adsorbed water and carbonate-related surface species. Quantitative analysis indicates a higher fraction of non-lattice oxygen species (O_{II} + O_{III}) in the NiBaRh catalyst compared with NiBa. In particular, Rh-containing samples show a larger relative contribution of the O_{II} component, suggesting an increased fraction of defective or interfacial oxygen species on the catalyst surface. This observation indicates that Rh incorporation modifies the surface oxygen environment and promotes the formation of more labile oxygen species associated with interfacial metal–oxide environments. Such an increase in the O_{II} contribution is consistent with the formation of a larger population of Ni–O–Ba interfacial environments, which are expected to play a key role in the redox behavior of the catalyst. The role of Rh appears to be mainly related to facilitating hydrogen activation and promoting faster redox processes on the catalyst surface, which could influence the regeneration stage of the cyclic CO_2–SR process.

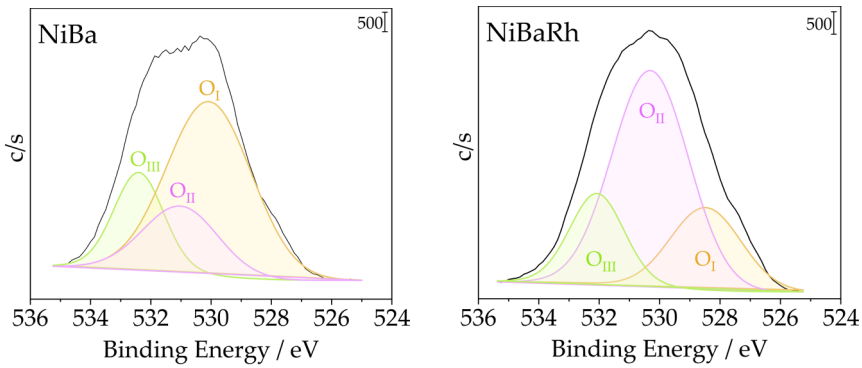


Figure 4. XPS spectra for the O 1s core-level region (black line) and deconvolution of NiBa 10/1 and NiBaRh 10/2/0.1 catalysts after calcination.

The structural and spectroscopic evidence obtained from XRD, Raman, H_2-TPR and XPS analyses indicates that the surface of these materials can be described in terms of a heterogeneous arrangement of several interacting domains. In particular, the results are consistent with the presence of three main types of surface environments: (i) interfacial Ni–O–Ba sites, arising from the intimate contact between Ni species and Ba-containing phases and characterized by relatively labile oxygen species; (ii) surface Ba–O–Ba domains, which provide the basic sites responsible for CO_2 adsorption and carbonate formation; and (iii) more extended BaO domains, capable of stabilizing more strongly bound carbonate species. Although these environments cannot be directly resolved as distinct phases, their presence can be inferred from the combined structural, redox and surface spectroscopic signatures observed for the catalysts.

Figure 5 presents the FTIR study of CO adsorption at liquid nitrogen temperature on preactivated NiBa 10/1 and NiBaRh 10/2/0.1 samples. Before CO exposure, both catalysts were outgassed under vacuum at 500 °C to remove pre-adsorbed species and generate clean, reduced surfaces. The spectra were recorded at −110 °C under 10 Torr of CO and subsequently during controlled outgassing up to room temperature, allowing the evolution of the adsorbed species to be monitored as a function of temperature. This experiment is designed to determine whether the catalyst surface possesses intrinsic oxidizing capability and to evaluate how

the mobility and reactivity of surface oxygen species evolve with temperature during CO adsorption and subsequent outgassing. At −110 °C, both samples exhibit two well-defined absorption bands in the 2200–2100 cm^{-1} region, corresponding to linearly adsorbed CO on metallic Ni sites. In NiBa, these bands appear at 2170 and 2150 cm^{-1}, while in NiBaRh they are observed at 2168 and 2185 cm^{-1}, reflecting the presence of distinct adsorption environments. As temperature increases, the CO bands in both materials progressively decrease in intensity, indicating gradual CO desorption during evacuation [30].

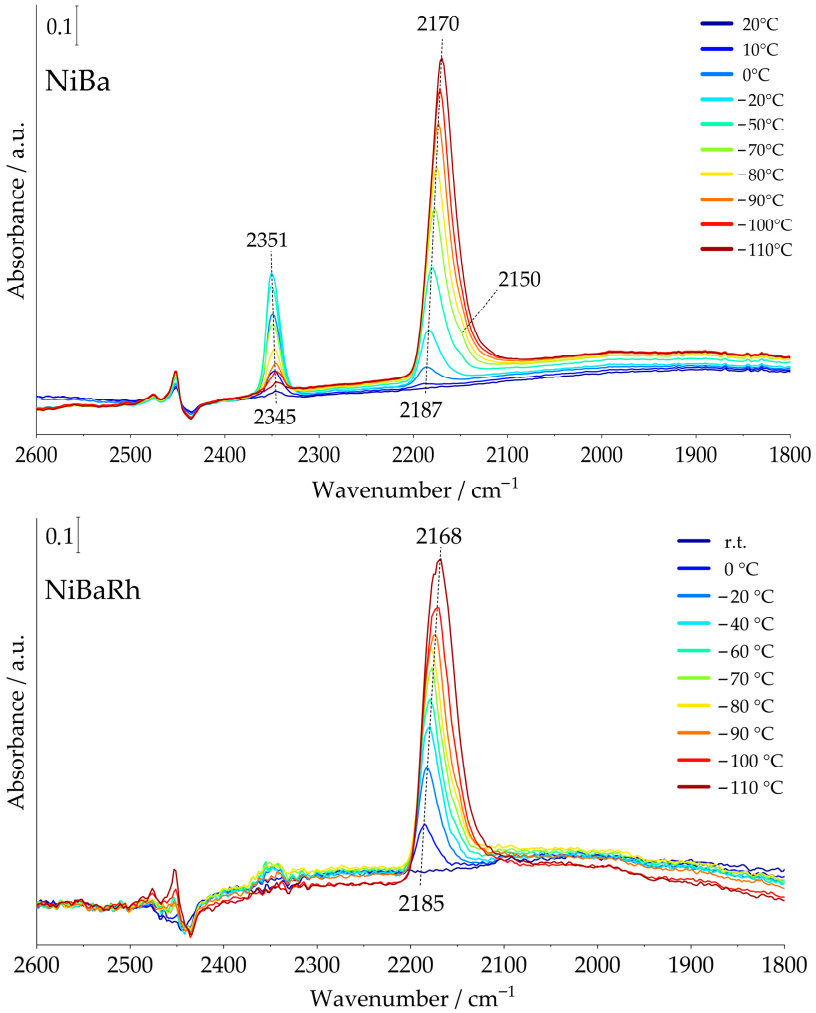


Figure 5. CO adsorption at liquid nitrogen temperature on preactivated NiBa 10/1 and NiBaRh 10/2/0.1 samples under vacuum at 500 °C. FTIR spectra were recorded at −110 °C in the presence of 10 Torr of CO and during subsequent outgassing up to room temperature.

A clear divergence between the two catalysts emerges during this thermal evolution. In NiBa, the disappearance of the CO bands is accompanied by the growth of new absorptions at 2351 and 2345 cm^{-1}, characteristic of CO_2 species stabilized on the surface [31]. The simultaneous loss of CO and formation of CO_2 demonstrates that part of the adsorbed CO is oxidized. This transformation reveals the participation of reactive surface oxygen, which is sufficiently mobile and available at low temperature to transfer oxygen to CO and generate CO_2, indicating the presence of reactive surface oxygen capable of oxidizing adsorbed CO according to the reaction: $CO_{ads} + O^* \rightarrow CO_2$. The subsequent disappearance of the CO_2 bands at higher temperatures reflects the desorption of these weakly bound species.

In contrast, the NiBaRh sample shows no evidence of CO_2 formation throughout the outgassing sequence. The CO bands simply diminish with increasing temperature, without

the appearance of any absorptions in the CO_2 region. This behavior indicates that the incorporation of Rh suppresses or consumes the reactive surface oxygen required for CO oxidation, thereby preventing CO_2 formation under the conditions studied. Considering the very low temperature of the experiment, the absence of detectable CO_2 formation cannot be attributed to kinetic limitations but rather to a lower availability of reactive surface oxygen species capable of participating in the oxidation of adsorbed CO. The comparison between the two materials thus provides direct insight into how surface oxygen availability and mobility depend on composition and temperature, and how these factors govern the oxidative capacity of the catalytic surface.

This result clearly indicates that the difference between both catalysts arises from their structural organization and interfacial architecture, rather than from purely kinetic effects.

The CO_2 adsorption properties of the catalysts were first evaluated to determine the amount of CO_2 that can be stored on the Ba-derived basic sites. Table 3 summarizes the CO_2 storage capacity determined from the saturation curves at 600 °C of the activated catalyst in H_2 atmosphere together with the total adsorption at 25 °C and desorption capacity obtained from CO_2-TPD experiments. The data presented in the table indicate that the NiBa catalyst, with a 10/1 ratio, exhibits an adsorption capacity at room temperature of 0.198 mmol $CO_2 \cdot g_{cat}{}^{-1}$. In addition, the desorption capacity of the catalyst in TPD is 6.4 µmol $CO_2 \cdot g_{cat}{}^{-1}$, while the adsorption capacity at 600 °C reaches a value of 0.171 mmol $CO_2 \cdot g^{-1}$. These results indicate that the catalyst exhibits a CO_2 retention capacity approximately 30 times higher than its desorption capacity. The NiBaRh 10/2/0.1 catalyst, which possesses a Ni/Ba ratio of 5/1, equivalent to 17% Ba in the formulation and 1% Rh relative to Ni, exhibited an adsorption value of 0.283 mmol $CO_2 \cdot g_{cat}{}^{-1}$ at room temperature. This value is higher than that of the NiBa catalyst. Additionally, the desorption capacity of the NiBaRh catalyst was determined to be 9.2 µmol $CO_2 \cdot g_{cat}{}^{-1}$. This indicates that the increase in desorption capacity is similar to that of the system without Rh. However, the adsorption capacity at 600 °C reaches a value of 0.17 mmol $CO_2 \cdot g_{cat}{}^{-1}$ in both catalysts. The small difference between the two materials suggests that the incorporation of Rh does not substantially modify the density of Ba-derived basic sites responsible for CO_2 capture, despite the fact that the NiBa ratio is twice as high for the catalyst containing Rh.

Table 3. CO_2 storage capacity calculated from the accumulation step at 600 °C and desorption capacity calculated from total CO_2-TPD measurements.

	Adsorption Capacity at 25 °C * mmol $CO_2 \cdot g_{cat}{}^{-1}$	**Desorption Capacity (25–800 °C) * µmol $CO_2 \cdot g_{cat}{}^{-1}$**	**Adsorption Capacity at 600 °C ** mmol $CO_2 \cdot g_{cat}{}^{-1}$**
NiBa 10/1	0.198	6.4	0.171
NiBaRh 10/2/0.1	0.283	9.2	0.169

* From CO_2-TPD and ** from saturation curve at 600 °C after reduction in 3% H_2/He for 1 h.

Considering the moderate specific surface areas of the catalysts (Table 1), the measured CO_2 uptake is consistent with the formation of surface carbonate species associated with Ba–O–Ba domains, corresponding to a partial coverage of the accessible Ba sites approaching monolayer-like carbonate formation. The presence of Rh therefore appears to have a limited influence on the intrinsic CO_2 adsorption capacity of the material. Instead, the Rh promoter may primarily affect the local structural organization of the catalyst, contributing to the stabilization of Ni species within Ba-containing environments and modifying the metal–oxide interfacial structure. Such effects are consistent with the evidence obtained from TPR and XPS analyses, which indicate changes in the reducibility and electronic environment of Ni in the Rh-containing catalyst.

The dynamic behavior of the catalysts under cyclic reaction conditions was investigated through transient pulse experiments performed at 600 °C, using alternating square

pulses of CO_2 and CH_4 (10,000 ppm) separated by intermediate helium purge steps, while the evolution of the gas-phase species was monitored by online mass spectrometry (MS).

In these experiments, the catalyst was first exposed to a CO_2 pulse to promote the storage of CO_2 on the catalyst surface. This step was followed by a helium purge, which removed weakly adsorbed or gas-phase species from the reactor. Subsequently, a CH_4 pulse was introduced to induce the regeneration of the material and the release of gaseous products formed during the interaction of methane with the CO_2-loaded catalyst surface. This sequence was repeated several times until stable cyclic behavior was obtained. Figure 6 shows the temporal evolution of the main gaseous species detected by MS (CO_2, CO, H_2 and CH_4) during representative cycles obtained for the NiBa 10/1 and NiBaRh 10/2/0.1 catalysts at 600 °C. The amounts of gaseous products discussed below were estimated by integrating the calibrated MS signals over the duration of the corresponding pulses and normalizing the results to the catalyst mass.

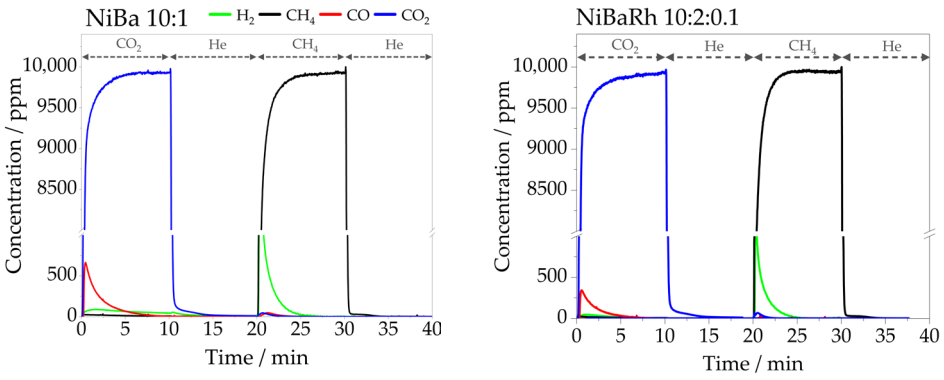


Figure 6. Gas evolution (CO_2, CH_4, CO and H_2) in transient CO_2–CH_4 cyclic response of NiBa 10/1 and NiBaRh 10/2/0.1 catalysts at 600 °C under alternating pulses of 10,000 ppm CO_2 and 10,000 ppm CH_4 in He.

During the CO_2 pulse, a rapid increase in the CO_2 signal is observed; as the pulse progresses, the intensity of the CO_2 signal increases until saturation, indicating the progressive capture of CO_2 on the catalyst surface. This reflects the interaction of CO_2 with the basic sites associated with Ba-containing surface domains, which are responsible for the storage of CO_2 in the form of carbonate species. At the beginning of the CO_2 pulse, a small transient formation of CO is also detected for both catalysts. This observation indicates that a fraction of the incoming CO_2 interacts with catalytic sites capable of promoting its partial activation. The integrated amounts of CO formed during this stage reach approximately 0.094 mmol·g^{-1} for NiBa 10/1 and 0.051 mmol·g^{-1} for NiBaRh 10/2/0.1, suggesting that the Ni-containing surface sites participate in the interaction between CO_2 and the catalyst surface.

The storage of CO_2 on these catalysts occurs mainly through the formation of carbonate species on Ba-derived basic sites. This process can be described by the reaction:

$$BaO + CO_2 \rightarrow BaCO_3$$

and may also involve surface basic pairs such as Ba–O–Ba, where CO_2 can be stabilized as bridging carbonate species. However, the transient profiles reveal that the storage stage cannot be described solely as a simple acid–base carbonatation process. During the initial moments of the CO_2 pulse, a transient formation of CO is detected in both catalysts, being twice as high for the catalyst that does not contain Rh. This indicates that a fraction of the

incoming CO_2 undergoes catalytic activation at metallic or interfacial sites, according to the partial dissociation of CO_2 on Ni-containing sites:

$$CO_2 + Ni \rightarrow CO + Ni–O$$

where the resulting oxygen species can be stabilized at the metal–oxide interface, forming Ni–O–Ba interfacial structures. The transient evolution of water observed towards the end of the CO_2 pulse suggests that part of this surface oxygen can react with hydrogen species present on the catalyst surface, producing H_2O. The delayed appearance of water indicates that the oxygen species generated during CO_2 activation accumulate temporarily on the surface before participating in subsequent reactions.

After the CO_2 pulse, the helium purge step removes the remaining gas-phase species from the reactor, restoring the baseline of the MS signals. When the feed is subsequently switched to CH_4, the system enters the regeneration stage of the cycle. During this pulse, clear transient signals of H_2 and CO are detected together with smaller amounts of CO_2, indicating that several reactions occur simultaneously during the interaction of methane with the previously CO_2-loaded catalyst surface.

A notable difference between the two catalysts is observed in the hydrogen formation during the CH_4 pulse. The NiBa 10/1 catalyst exhibits a more intense H_2 signal, corresponding to a total hydrogen production of approximately 0.112 mmol·g^{-1}, whereas the NiBaRh 10/2/0.1 catalyst shows a lower hydrogen signal, corresponding to approximately 0.079 mmol·g^{-1}. These results indicate that both catalysts are capable of activating methane under these conditions, although the extent of hydrogen formation differs between the two materials.

In contrast to the storage stage, the formation of hydrogen occurs exclusively during the CH_4 pulse, confirming that hydrogen is generated through methane activation on metallic sites:

$$CH_4 \rightarrow C^* + 2H_2$$

The carbon species generated during methane dissociation may subsequently react with the carbonate species formed during the storage stage, regenerating the basic Ba sites and alternatively, carbonate species may also react directly with methane through reactions such as:

$$BaCO_3 + C^* \rightarrow BaO + 2CO$$

$$BaCO_3 + CH_4 \rightarrow BaO + 2CO + H_2 + H_2O$$

These processes account for the simultaneous formation of CO, H_2 and H_2O observed during the regeneration pulse. In addition, part of the CO_2 released from carbonate decomposition can react with methane through dry reforming $CH_4 + CO_2 \rightarrow 2CO + 2H_2$. The relative contribution of these pathways determines the H_2/CO ratio observed during the regeneration stage. For instance, the catalyst NiBa 10/1 exhibits an H_2/CO ratio of 3.95, which is consistent with the coexistence of methane dissociation and dry reforming reactions. In contrast, the Rh-promoted catalyst NiBaRh 10/2/0.1 shows a significantly higher H_2/CO ratio, around 15.8, suggesting that the presence of Rh reduces the relative contribution of CO-forming pathways.

The comparison between both catalysts suggests that the Ni/Ba ratio may influence the availability of Ni-containing sites involved in the interaction with CO_2 and CH_4 during the cyclic process, while the Ba surface domains govern the CO_2 storage capacity of the materials. These observations indicate that the cyclic behavior results from the combined contribution of Ba-based storage sites and Ni-containing catalytic sites, whose relative distribution depends on the catalyst composition. To further clarify the influence of catalyst composition on the CO_2-SR process, two additional model catalysts were prepared. A NiBa 1/1 catalyst was synthesized to

evaluate the effect of a higher Ba/Ni ratio on CO_2 storage and carbonate stability. In addition, a NiBaRh 10/1/0.1 catalyst was obtained by Rh impregnation over the NiBa 10/1 material, allowing the effect of Rh surface enrichment to be evaluated without significantly modifying the bulk composition of the Ni–Ba system. In this way, two key parameters governing the cyclic process can be examined independently: the relative abundance of Ba-derived storage sites, controlled by the Ni/Ba ratio, and the surface accessibility of Rh species, which may influence hydrogen activation and the reducibility of the Ni-containing phases. The catalysts were characterized by XRD, surface area measurements and XPS analysis, and their catalytic activity was subsequently evaluated under the same cyclic CO_2-SR conditions. Some relevant results are summarized in Table 4.

Table 4. Morphological and structural properties of the NiBaRh 10/1/0.1 and NiBa 1/1 catalysts. Ni/Rh and Ni/Ba surface ratios obtained from XPS.

	A_{BET} [a] $m^2 \cdot g^{-1}$	V_p [b] $cm^3 \cdot g^{-1}$	NiO Crystal Size [c] Å	Ni/Ba [d] -	Ni/Rh [d] -
NiBaRh 10/1/0.1	42	0.09	46.5	9.1	4.3
NiBa 1/1	28	0.09	259.5	4.1	-

[a] calculated by BET equation, [b] BET adsorption pore volume, [c] average crystalline diameter using Rietveld refinement from XRD and [d] from XPS measurements.

Surface analysis by XPS indicates that Rh introduced by impregnation exhibits a higher surface concentration than Rh incorporated by co-precipitation, implying that Rh species are preferentially located at the external surface of the catalyst particles since the Ni/Rh ratio obtained by XPS is lower (4.3). In agreement with the structural information obtained by XRD, the Rh-impregnated catalyst also exhibits a markedly smaller NiO crystallite size, around 46 Å, whereas the remaining catalysts show significantly larger values in the range of 230–260 Å. The decrease in NiO crystallite size indicates a higher dispersion of the nickel phase and consequently a larger metal–oxide interfacial area. This structural feature is particularly relevant in these unsupported catalysts, where the catalytic activity is largely governed by processes occurring at the external surface and at the metal–oxide interfaces. This structural modification has important consequences for the CO_2 storage–regeneration cycle. Smaller NiO domains increase the density of Ni–Ba interfacial sites, where CO_2 activation and carbonate formation occur. This effect is reflected in the measured CO_2 storage capacities. The NiBa 10/1 catalyst, characterized by NiO crystallites of approximately 250 Å, exhibits CO_2 storage capacities close to 0.171 mmol $CO_2 \cdot g^{-1}$. In contrast, the Rh-promoted catalyst NiBaRh 10/1/0.1, which presents significantly smaller NiO crystallites of about 4.5 nm (≈46 Å), reaches slightly higher values around 0.181 mmol $CO_2 \cdot g^{-1}$.

The comparison between both systems indicates that the reduction in the NiO crystallite size increases the effective CO_2 storage capacity, not primarily through an increase in the BET surface area, but rather through an increase in the density of defective surface domains associated with nanocrystalline phases.

In the case of the Rh-containing catalysts, the presence of surface Rh species, as evidenced by XPS, acts as an additional promoter. Rh facilitates hydrogen activation and hydrogen spillover processes, which enhance the reducibility of NiO and of the mixed Ni–Ba interfacial species. This fact is consistent with the shift toward lower reduction temperatures observed in the H_2-TPR profiles and contributes to a more efficient activation of methane during the regeneration stage. Therefore, Rh not only modifies the surface redox environment but also promotes the dynamic processes associated with carbonate formation and decomposition at the metal–oxide interface.

The influence of the Ba content becomes particularly evident in the NiBa 1/1 catalyst; structural characterization by XRD reveals a stronger contribution of carbonate-related

phases, while XPS analysis also indicates a larger fraction of surface carbonate species compared with the catalysts containing lower Ba loadings. These results suggest that higher Ba concentration favors the formation and stabilization of Ba carbonates. However, despite this higher carbonate abundance, the dynamically accessible CO_2 storage capacity under cyclic conditions becomes limited. This indicates that a significant fraction of the formed carbonates is too stable to be efficiently decomposed during the methane regeneration pulse. Therefore, although carbonate formation is thermodynamically favored in Ba-rich systems, its high stability reduces the reversibility of the storage–release cycle and limits the effective amount of CO_2 that can participate in the catalytic process.

The isothermal activity of the catalysts during the CO_2 storage–reduction (CO_2-SR) process was also investigated on the two additional NiBa 1/1 and NiBaRh 10/1/0.1 model catalysts. The evolution of the main gaseous species detected during a representative cycle is shown in Figure 7 for the four catalysts investigated: NiBa 10/1, NiBaRh 10/2/0.1, NiBaRh 10/1/0.1 and NiBa 1/1. The profiles correspond to steady cycles obtained after several repetitions of the pulse sequence. Although general cyclic behavior is similar for the four materials, clear differences in the intensity and temporal evolution of the signals can be observed. In particular, the relative intensity of the H_2 and CO signals during the methane pulse varies significantly depending on the catalyst composition, revealing differences in the dominant reaction pathways involved in the regeneration step. These variations become clearer when the transient signals are quantified through integration of the steady-state cycles. The resulting values are summarized in Table 5, which also includes the H_2/CO ratio measured during the regeneration stage.

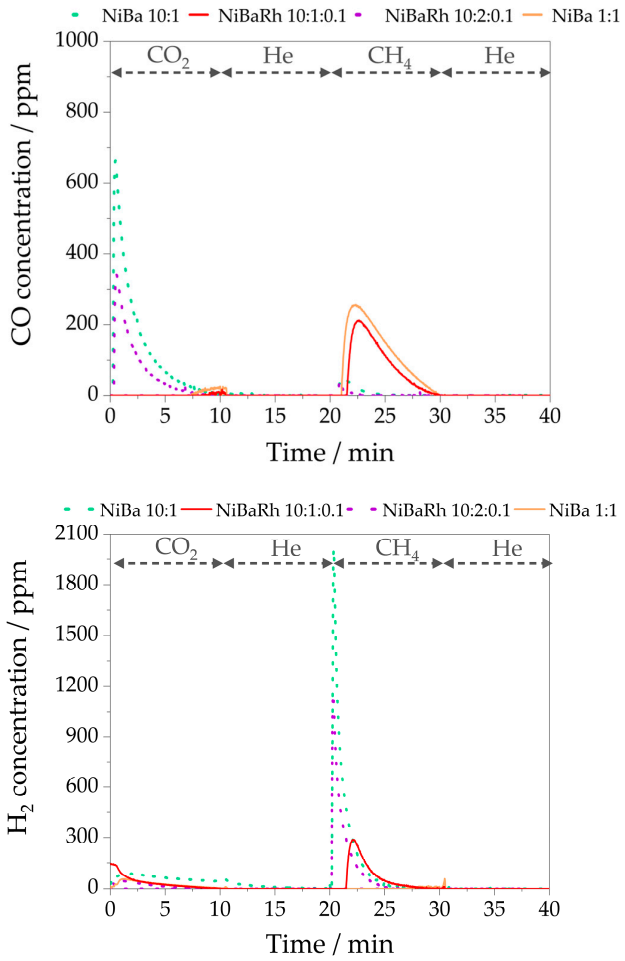


Figure 7. *Cont.*

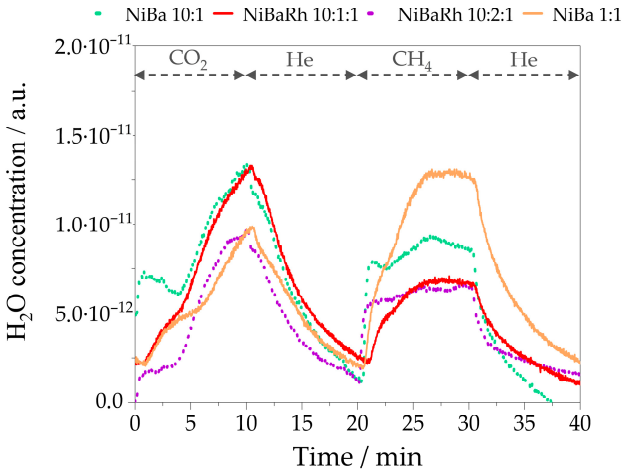


Figure 7. Concentration profiles of CO, H_2 and H_2O during one CO_2–CH_4 cycle over NiBa 10/1, NiBaRh 10/2/0.1, NiBa 10/1/0.1 and NiBa 1/1 catalysts at 600 °C under alternating pulses of 10,000 ppm CO_2 and 10,000 ppm CH_4 in He, separated by intermediate He purges.

Table 5. Catalytic performance of NiBa 10/1, NiBaRh 10/2/0.1, NiBa 10/1/0.1 and NiBa 1/1 during cyclic CO_2–CH_4 operation at 600 °C, including CH_4 conversion, CO_2 storage capacity and H_2/CO ratio.

	CO_2 Cycle		CH_4 Cycle	
	mmol $CO_2 \cdot g^{-1}_{cat}$	X_{CO2}	H_2/CO	X_{CH4}
NiBa 10/1	0.146	1.84	3.95	3.21
NiBaRh 10/2/0.1	0.159	2.06	15.8	2.86
NiBaRh 10/1/0.1	0.230	2.81	0.81	2.69
NiBa 1/1	0.253	2.87	0.07	2.40

The results indicate that the CO_2 storage capacity depends strongly on the catalyst composition, particularly on the Ni/Ba ratio and the dispersion of the metallic phase. The reference catalyst NiBa 10/1 exhibits a CO_2 removal (stored + converted) capacity of 0.146 mmol·g^{-1}, which is consistent with the formation of carbonate species on Ba-derived surface basic sites. A slightly higher value is obtained for NiBaRh 10/2/0.1, indicating that the presence of Rh does not significantly modify the density of Ba basic sites responsible for CO_2 uptake. A much larger increase in CO_2 storage is observed for NiBaRh 10/1/0.1, which reaches 0.230 mmol·g^{-1}. This suggests that the surface enrichment of Rh introduced by impregnation together with the higher dispersion of the Ni phase increases the density of Ni–Ba interfacial sites capable of stabilizing CO_2-derived species. These interfacial environments appear to play a key role in the reversible interaction between CO_2 and the catalyst surface. The Ba-rich catalyst NiBa 1/1, although containing a higher Ba content, exhibits a larger dynamically accessible storage capacity (0.253 mmol $CO_2 \cdot g^{-1}$) under cyclic conditions. This observation indicates that CO_2 storage in these materials is not governed solely by the total Ba loading, but rather by the availability of surface basic sites and mixed Ni–Ba interfacial environments that can reversibly form and decompose carbonates.

The fraction of dynamically accessible Ba sites was evaluated by comparing the measured CO_2 uptake with the theoretical capacity based on the total Ba content, assuming a 1:1 stoichiometry between Ba and CO_2 during carbonate formation ($BaO + CO_2 \rightarrow BaCO_3$). For the NiBa catalysts studied, the experimental CO_2 uptakes (0.146 and 0.253 mmol $CO_2 \cdot g^{-1}$) correspond to roughly 10–20% of the total Ba sites, indicating that only a fraction of Ba is actively involved in the reversible carbonation process. When expressed in terms of surface coverage, these uptakes correspond to ~26% of the available surface area for the

catalyst with higher BET (55 $m^2 \cdot g^{-1}$) and ~87% for the lower BET catalyst (28 $m^2 \cdot g^{-1}$). This comparison highlights that the CO_2 adsorption is not limited by the total surface area alone but is strongly influenced by the distribution and accessibility of Ba sites, particularly at Ni–Ba interfacial environments capable of participating in reversible carbonate formation and decomposition.

The product distribution during the regeneration stage further reflects these structural differences. The NiBa 10/1 catalyst exhibits an H_2/CO ratio close to 4, which is consistent with the coexistence of methane dissociation and dry reforming pathways. In contrast, the Rh-promoted catalyst NiBaRh 10/2/0.1 shows a much higher H_2/CO ratio (15.8), indicating that Rh promotes methane activation and hydrogen formation, likely through hydrogen spillover processes that enhance the reducibility of Ni-containing sites. For the NiBaRh 10/1/0.1 catalyst, the H_2/CO ratio decreases to 0.81, suggesting a larger contribution of CO-forming pathways, as dry reforming reaction, associated with the activation of CO_2 at Ni–Ba interfacial sites, or the inhibition of side reactions as methane decomposition. Finally, the Ba-rich catalyst NiBa 1/1 exhibits a very low H_2/CO ratio (0.07), indicating that carbonate species formed in this material are significantly more stable and are less efficiently decomposed during the methane pulse. Although carbonate formation is thermodynamically favored in Ba-rich systems, its high stability reduces the reversibility of the cycle.

To summarize, the transient profiles, the product distributions and the integrated catalytic data indicate that the CO_2-SR process proceeds through a surface-controlled mechanism involving reversible carbonate formation on Ba-derived basic sites coupled with catalytic activation processes occurring at Ni-containing interfacial sites. The amount of CO_2 stored corresponds to a surface or sub-monolayer coverage of carbonate species, which correlates with the surface density of basic Ba sites and mixed Ni–Ba interfacial domains.

Within this framework, the cyclic CO_2-SR process can be described as a dynamic sequence in which CO_2 is temporarily retained at the catalyst surface as carbonate species, while Ni-based sites activate methane and promote the regeneration of the Ba-based storage domains. The efficiency of the cycle therefore depends on the balance between the CO_2 storage capacity and the ability of the catalyst to regenerate the carbonate species during the methane pulse. The results indicate that optimal CO_2-SR performance is achieved when a balanced distribution of Ba-derived basic sites and Ni-containing interfacial sites are present, allowing reversible carbonate formation while maintaining efficient methane activation. In this context, the Ni/Ba ratio controls the density and stability of the carbonate domains, whereas the presence and dispersion of Rh influence the redox behavior and methane activation during the regeneration stage. These findings provide useful guidelines for the design of improved catalysts for cyclic CO_2 capture and conversion processes.

The catalyst surface comprises a hierarchical distribution of three types of domains. First, Ni–O–Ba interfacial sites formed at the boundary between Ni particles and adjacent Ba-containing regions provide catalytically active centers for CO_2 activation, oxygen stabilization, and methane-induced regeneration, with their density increasing for highly dispersed Ni. Second, surface Ba–O–Ba sites act as reversible CO_2 storage domains, stabilizing labile carbonate species that can be efficiently decomposed during the regeneration step. Third, extended Ba-rich aggregates favor strongly stabilized carbonates that are less reactive, reducing the dynamic accessibility of stored CO_2. The Ni/Ba ratio controls the relative abundance of these domains, with moderate Ba contents enabling an optimal balance between CO_2 storage and catalytic regeneration, whereas excessive Ba promotes inert carbonate formation. Additionally, Rh promotes Ni dispersion, hydrogen activation, and Ni–Ba interfacial density, enhancing the coupling between storage and catalytic functions. Overall, the CO_2-SR process operates as a dynamic surface cycle at sub-monolayer

carbonate coverage, where reversible Ba-based storage sites and active Ni–Ba interfaces must be balanced to maximize cyclic CO_2 uptake and catalyst regeneration.

3. Materials and Methods

3.1. Catalyst Preparation

Four unsupported catalysts were synthesized for this study, NiBa 10/1, NiBaRh 10/2/0.1, NiBa 10/1/0.1, and NiBa 1/1, where the numbers indicate the nominal atomic ratios of NiBaRh. The NiBa 10/1 and NiBa 1/1 catalysts were prepared by co-precipitation of the corresponding metal nitrates in aqueous medium. Nickel nitrate hexahydrate ($Ni(NO_3)_2{\cdot}6H_2O$) and barium nitrate ($Ba(NO_3)_2$) were dissolved in deionized water according to the desired atomic ratio. An aqueous ammonia solution was added dropwise under continuous stirring until complete precipitation was achieved. Subsequently, 3 wt.% of LUDOX HS-40 colloidal silica was incorporated as a nucleating agent and surface promoter. The resulting suspension was stirred overnight at room temperature and then subjected to three sonication cycles of 15 s each using an ultrasonic processor UIP 1000 hd (Hielscher, Teltow, Germany) equipped with a titanium sonotrode operating at 20 kHz and 300 W cm^{-2}. The NiBaRh 10/2/0.1 catalyst, corresponding to a Ni/Ba atomic ratio of 5/1 and a Ni/Rh atomic ratio of 100/1, was synthesized by simultaneous co-precipitation of $Ni(NO_3)_2{\cdot}6H_2O$, $Ba(NO_3)_2$, and $Rh(NO_3)_3{\cdot}xH_2O$ following the same procedure described above, adjusting the precursor concentrations to obtain the targeted atomic ratios. The NiBa 10/1/0.1 catalyst was prepared by wet impregnation of Rh onto the previously calcined NiBa 10/1 solid. An aqueous solution of $Rh(NO_3)_3{\cdot}xH_2O$ was added dropwise to the NiBa 10/1 powder under stirring to achieve the desired Ni/Rh atomic ratio. The impregnated solids were dried prior to calcination. All solids were washed thoroughly with deionized water, recovered by ultracentrifugation, dried at 100 °C overnight, and finally calcined in static air at 800 °C for 4 h.

3.2. Characterization

3.2.1. Textural Properties

Nitrogen adsorption–desorption isotherms were recorded at −196 °C using a Micromeritics ASAP 2020 analyzer (Norcross, GA, USA). Prior to analysis, samples were degassed under vacuum at 80 °C until a residual pressure below 10^{-3} Pa was reached. The specific surface area was calculated using the Brunauer–Emmett–Teller method, and the pore volume was estimated from the adsorption branch using the Barrett–Joyner–Halenda model.

CO_2 adsorption isotherms at 25 °C were also measured using the same instrument after identical degassing treatment.

3.2.2. X-Ray Diffraction

Powder X-ray diffraction patterns were collected over the 2theta range 10–80 degrees on an X'Pert Pro MPD diffractometer (PANalytical, Malvern, UK) using CuKα1 radiation with a wavelength of 1.5406 Å and a Ge(111) monochromator. Diffraction patterns were recorded for both calcined and H_2-reduced samples when specified. The size of the NiO crystallite was calculated using the Williamson–Hall approach implemented within a Rietveld refinement.

3.2.3. X-Ray Photoelectron Spectroscopy

X-ray photoelectron spectroscopy measurements were performed on a PHI 04-584 spectrometer (Chanhassen, MN, USA) equipped with Al Kα radiation at 1486.6 eV and a dual-beam charge neutralizer. Binding energies were referenced to the C 1s peak at

284.8 eV with an uncertainty of ±0.2 eV. Spectral deconvolution was carried out using Gaussian–Lorentzian functions with a mixing ratio between 60 and 80 percent.

3.2.4. Raman Spectroscopy

Raman spectra were recorded at room temperature using a DXR Raman microscope (Thermo Scientific, Waltham, MA, USA) equipped with a 532 nm excitation laser operating at 7 mW and a CCD detector. Spectra were collected in the range 100–2000 cm^{-1}. Measurements were performed on both calcined and reduced samples when indicated.

3.2.5. CO_2 Temperature-Programmed Desorption and H_2 Temperature-Programmed Reduction

CO_2 temperature-programmed desorption and H_2 temperature-programmed reduction experiments were carried out using a Micromeritics AutoChem III system. For CO_2 temperature-programmed desorption, samples were pretreated in helium at 800 °C for 1 h, cooled to 60 °C, and saturated with CO_2. Subsequently, the temperature increased to 800 °C at a heating rate of 30 °C min^{-1} under helium flow.

H_2 temperature-programmed reduction was performed under 10 percent H_2 in Ar from room temperature to 800 °C at 10 °C min^{-1}.

3.2.6. Transient CO_2 Adsorption Measurements

CO_2 adsorption experiments were conducted in a U-shaped fixed-bed quartz reactor coupled to a Pfeiffer Prisma QMS 200 mass spectrometer (Aßlar, Germany). Approximately 60 mg of catalyst was loaded into the reactor and pretreated under 3 percent H_2 in He at 600 °C for 1 h. After stabilization under helium, rectangular pulses of 2000 ppm CO_2 in He were introduced at 600 °C with a total flow rate of 100 mL min^{-1}. CO_2 uptake was calculated from integrated CO_2 signals during a rectangular pulse using Equation (1) where F represents the total fed volumetric gas flow:

$$CO_2^{stored}(mmol_{CO_2} \cdot g_{cat}^{-1}) = \frac{A_{CO_2\ retained} \cdot F}{g_{cat}} \quad (1)$$

3.3. Infrared Spectroscopy

Fourier transform infrared spectra were recorded using a Nicolet Nexus 380 spectrometer (Thermo Fisher Scientific, Waltham, MA, USA). Self-supported wafers containing 15–20 mg of sample were placed in an in situ IR cell connected to a high-vacuum line. Prior to adsorption experiments, samples were activated under high vacuum at 500 °C and then cooled to the desired temperature. CO adsorption experiments were performed at −110 °C. Spectra were recorded after successive adsorption and outgassing steps, followed by gradual heating to room temperature. For each spectrum, 100 scans were collected with a resolution of 4 cm^{-1}.

3.4. Catalytic Activity

Cyclic CO_2 storage and CH_4 regeneration experiments were carried out at 600 °C and atmospheric pressure using a transient response methodology in a fixed-bed quartz reactor coupled to a Pfeiffer Prisma QMS 200 mass spectrometer. In each cycle, 10,000 ppm of CO_2 in He was introduced for 10 min, followed by a 10 min helium purge. Subsequently, 10,000 ppm of CH4 in He was fed for 10 min, followed by another 10 min helium purge. The total inlet flow was 100 mL min^{-1}, corresponding to a gas hourly space velocity of $2.12 \cdot 10^4$ h^{-1} with 60 mg of catalyst. Prior to reaction, the catalyst was reduced in situ under 3 percent H_2 in He at 600 °C for 1 h and purged with helium until a stable baseline was achieved. Blank experiments under identical conditions were conducted

without catalyst, to verify the absence of homogeneous or reactor-related contributions. Mass signals corresponding to H_2, He, CH_4, H_2O, CO, O_2, and CO_2 were continuously monitored and calibrated to minimize fragmentation interferences.

4. Conclusions

This work investigated the relationship between structural properties and dynamic catalytic performance in unsupported Ni–Ba catalysts applied to the cyclic CO_2 storage–regeneration (CO_2-SR) process under alternating CO_2–CH_4 operation. The results demonstrate that the catalytic performance of these materials is not determined simply by the overall Ba content, but rather by the structural organization of the Ni–Ba interface and the stability of the carbonate species formed during operation. Combined structural, spectroscopic and transient analyses indicate that these catalysts exhibit a hierarchical surface organization composed of three main types of domains: dynamic Ni–O–Ba interfacial sites, Ba–O–Ba surface domains responsible for CO_2 adsorption and carbonate formation, and more extended Ba-rich domains capable of stabilizing strongly bound carbonates. The distribution of these domains governs the effective basicity of the system, the mobility of oxygen species and the reversibility of carbonate formation during the cyclic CO_2-SR process.

Under the studied conditions, CO_2 storage occurs predominantly via carbonate formation corresponding to mono- or sub-monolayer coverage on Ba-derived surface sites. Only a fraction (~10–20%) of the total Ba sites is dynamically involved in the reversible carbonation process, reflecting the presence of distinct surface domains and interfacial Ni–Ba environments. The CO_2 storage capacity is not governed solely by the total Ba content, but also by surface accessibility. The Ni/Ba ratio controls the balance between reversible carbonate formation and catalyst regeneration. Catalysts with Ni/Ba $\approx$ 10 favor the formation of Ni–O–Ba interfacial domains that combine CO_2 adsorption capacity with sufficient redox flexibility to enable efficient carbonate regeneration during the methane pulse. In contrast, catalysts with higher Ba contents stabilize larger amounts of carbonate species associated with Ba-rich domains, which limits the reversibility of the cyclic process and reduces the dynamically accessible CO_2 storage.

Rhodium promotion (Ni/Rh $\approx$ 100) mainly modifies the redox dynamics of the catalysts. Rh species, preferentially located at the outer surface when introduced by impregnation, enhance reducibility and facilitate hydrogen activation through hydrogen spillover, thereby accelerating the regeneration of carbonate species during the reduction stage without significantly altering the intrinsic CO_2 storage capacity of Ba-derived basic sites.

Transient experiments under alternating CO_2 and CH_4 pulses demonstrate that the CO_2-SR process operates through a dynamic surface cycle in which CO_2 is temporarily stored as carbonate species on Ba-derived domains while methane activation occurs on Ni-containing interfacial sites. The cyclic alternation between storage and regeneration continuously restores the active surface domains and enables the conversion of CO_2 and CH_4 into H_2 and CO, allowing operation beyond the thermodynamic limitations that typically affect steady-state CO_2 conversion processes.

These results highlight the importance of controlling Ni–Ba interfacial domains and oxygen mobility for the rational design of multifunctional catalysts capable of coupling cyclic CO_2 capture and catalytic conversion in CO_2-SR processes.

Author Contributions: S.E.-M.: Data curation, Investigation, Methodology, Writing—original draft. S.M.-R.: Data curation, Investigation, Methodology. M.C.-R.: Data curation, Formal analysis, Investigation, Methodology, Validation, Writing—review and editing. C.H.: Conceptualization, Formal analysis, Funding acquisition, Investigation, Project administration, Writing—original draft, Writing—review and editing. E.F.: Data curation, Formal analysis, Investigation. M.Á.L.: Conceptualization, Formal analysis, Funding acquisition, Investigation, Project administration, Supervision,

Writing—review and editing. L.J.A.: Conceptualization, Data curation, Formal analysis, Investigation, Methodology, Supervision, Validation, Writing—review and editing. All authors have read and agreed to the published version of the manuscript.

Funding: This research was funded by the Spanish Ministry of Science, Innovation and Universities under Project PID2021-124098OB-I00.

Data Availability Statement: Data will be available on request.

Acknowledgments: The authors acknowledge the financial support of from the Spanish Ministry of Science, Innovation and Universities (PID2021-124098OB-I00). SEM acknowledges the research fellowship provided by the University of Malaga.

Conflicts of Interest: The authors declare no conflicts of interest. The funders had no role in the design of the study; in the collection, analyses, or interpretation of data; in the writing of the manuscript; or in the decision to publish the results.

References

1. Sun, H.; Sun, S.; Liu, T.; Zeng, J.; Wang, Y.; Yan, Z.; Wu, C. Integrated CO_2 Capture and Utilization: Selection, Matching, and Interactions between Adsorption and Catalytic Sites. *ACS Catal.* **2024**, *14*, 15572–15589. [CrossRef]
2. Qiao, Y.; Liu, W.; Guo, R.; Sun, S.; Zhang, S.; Bailey, J.J.; Fang, M.; Wu, C. Techno-Economic Analysis of Integrated Carbon Capture and Utilisation Compared with Carbon Capture and Utilisation with Syngas Production. *Fuel* **2023**, *332*, 125972. [CrossRef]
3. Sarmad, S.; Lu, D.; Gao, S.; Sun, Z.; Zhou, Z.; Ali, A.; Duan, L. Advancing Syngas Production: A Comparative Techno-Economic Analysis of ICCU and CCU Technologies for CO_2 Emission Reduction. *J. Environ. Chem. Eng.* **2024**, *12*, 114562. [CrossRef]
4. Sun, S.; Zhang, C.; Wang, Y.; Zhao, X.; Sun, H.; Wu, C. CO_2 Capture from H_2O and O_2 Containing Flue Gas Integrating with Dry Reforming Methane Using Ni-Doping CaO Dual Functional Materials. *Chem. Eng. J.* **2023**, *468*, 143712. [CrossRef]
5. Sun, S.; Zhang, Y.; Li, C.; Wang, Y.; Zhang, C.; Zhao, X.; Sun, H.; Wu, C. Upgrading CO_2 from Simulated Power Plant Flue Gas via Integrated CO_2 Capture and Dry Reforming of Methane Using Ni-CaO. *Sep. Purif. Technol.* **2023**, *308*, 122956. [CrossRef]
6. Shao, B.; Wang, Z.-Q.; Gong, X.-Q.; Liu, H.; Qian, F.; Hu, P.; Hu, J. Synergistic Promotions between CO_2 Capture and In-Situ Conversion on Ni-CaO Composite Catalyst. *Nat. Commun.* **2023**, *14*, 996. [CrossRef] [PubMed]
7. Sun, S.; Wang, Y.; Xu, Y.; Sun, H.; Zhao, X.; Zhang, Y.; Yang, X.; Bie, X.; Wu, M.; Zhang, C.; et al. Ni-Functionalized Ca@Si Yolk-Shell Nanoreactors for Enhanced Integrated CO_2 Capture and Dry Reforming of Methane via Confined Catalysis. *Appl. Catal. B Environ. Energy* **2024**, *348*, 123838. [CrossRef]
8. Tian, S.; Yan, F.; Zhang, Z.; Jiang, J. Calcium-Looping Reforming of Methane Realizes In Situ CO_2 Utilization with Improved Energy Efficiency. *Sci. Adv.* **2019**, *5*, eaav5077. [CrossRef] [PubMed]
9. Sun, S.; Chen, Z.; Xu, Y.; Wang, Y.; Zhang, Y.; Dejoie, C.; Xu, S.; Xu, X.; Wu, C. Potassium-Promoted Limestone for Preferential Direct Hydrogenation of Carbonates in Integrated CO_2 Capture and Utilization. *JACS Au* **2024**, *4*, 72–79. [CrossRef]
10. Han, R.; Wang, Y.; Wei, L.; Peng, M.; Li, Z.; Liu, C.; Liu, Q. Integrated CO_2 Capture and Conversion by Cu/CaO Dual Function Materials: Effect of In-Situ Conversion on the Sintering of CaO and Its CO_2 Capture Performance. *Carbon Capture Sci. Technol.* **2024**, *12*, 100220. [CrossRef]
11. Gao, Z.; Yuan, Y.; Yang, P.; Hu, X.; Ma, J.; Ma, Q.; Guo, T.; Zhang, J.; Guo, Q. In Situ Capture and Conversion of CO_2 to CO Using $CaZrO_3$ Promoted Fe–CaO Dual-Functional Material. *ACS Sustain. Chem. Eng.* **2024**, *12*, 10933–10946. [CrossRef]
12. Tsiotsias, A.I.; Charisiou, N.D.; Yentekakis, I.V.; Goula, M.A. The Role of Alkali and Alkaline Earth Metals in the CO_2 Methanation Reaction and the Combined Capture and Methanation of CO_2. *Catalysts* **2020**, *10*, 812. [CrossRef]
13. Mader, N.; Mack, A.; Scheffknecht, G. CO_2 Capture for Backup Power Plants: Entrained Flow Calcium Looping Using $Ca(OH)_2$. *Fuel* **2025**, *401*, 135855. [CrossRef]
14. Molina-Ramírez, S.; Peltzer, D.; Cortés-Reyes, M.; Herrera, C.; Larrubia, M.A.; Cornaglia, L.; Alemany, L.J. CO_2-SR Technology Using NiBa Unsupported Catalyst. Isotopic Study of Cyclic Process of CO_2 Storage and In Situ Regeneration with CH_4. *Fuel* **2023**, *341*, 127690. [CrossRef]
15. Essounani-Mérida, S.; Molina-Ramírez, S.; Cortés-Reyes, M.; Herrera, C.; Larrubia, M.Á.; Alemany, L.J. Influence of Second Metal Incorporation on Nickel-Based Unsupported Catalysts for CO_2 Reduction (CO_2-SR) Technology. *Results Eng.* **2025**, *26*, 104921. [CrossRef]
16. Saadu Itas, Y.; Khandaker, M.U.; Mahmoud, M. Evaluating the CO_2 Capture Potential of MgO Sheets: A DFT Study on the Effects of Vacancy and Ni Doping for Assessing Environmental Sustainability. *RSC Adv.* **2025**, *15*, 3047–3059. [CrossRef] [PubMed]
17. Sharma, H.; Yadav, P.K.; Sharma, S.; Dhir, A. Dry-Oxidative Reforming of Biogas for Hydrogen Generation over Ca and Mg-Promoted Titania-Supported Nickel Catalyst. *Hydrogen* **2025**, *6*, 64. [CrossRef]

18. Sattari, O.; Nematollahi, B.; Rezaei, M.; Alavi, S.M. Effect of MgO on the Catalytic Activity and Stability of Nickel-Based Catalyst in Methane Dry Reforming Reaction. *Sci. Rep.* **2025**, *15*, 39649. [CrossRef]
19. Ocsachoque, M.A.; Leguizamon, M.S.; Gonzalez, M.G. Effect of Rh Addition to Ni/MgO-Al_2O_3 Catalysts for Dry Reforming of Methane. *Indian J. Sci. Technol.* **2017**, *10*, 1–9. [CrossRef]
20. Lee, J.A.; Bae, Y.; Hong, K.; Hong, J. Comparative Evaluation of Ni-Based Bimetallic Catalysts for Dry Reforming of Methane at Low Temperature: The Effect of Alloy Itself on Performance. *Int. J. Energy Res.* **2022**, *46*, 11228–11249. [CrossRef]
21. Saleh, J.; Al-Fatesh, A.S.; Ibrahim, A.A.; Frusteri, F.; Abasaeed, A.E.; Fakeeha, A.H.; Albaqi, F.; Anojaidi, K.; Alreshaidan, S.B.; Albinali, I.; et al. Stability and Activity of Rhodium Promoted Nickel-Based Catalysts in Dry Reforming of Methane. *Nanomaterials* **2023**, *13*, 547. [CrossRef] [PubMed]
22. Benner, R.E.; Mitchell, J.R.; Grow, R.W. Raman Scattering as a Diagnostic Technique for Cathode Characterization. *IEEE Trans. Electron. Devices* **1987**, *34*, 1842–1847. [CrossRef]
23. Kwan, J.T.H.; Bonakdarpour, A.; Afonso, G.; Wilkinson, D.P. Bridging Fundamental Electrochemistry with Applied Fuel Cell Testing: A Novel and Economical Rotating Disk Electrode Tip for Electrochemical Assessment of Catalyst-Coated Membranes. *Electrochim. Acta* **2017**, *258*, 208–219. [CrossRef]
24. Jeangros, Q.; Hansen, T.W.; Wagner, J.B.; Damsgaard, C.D.; Dunin-Borkowski, R.E.; Hébert, C.; Van Herle, J.; Hessler-Wyser, A. Reduction of Nickel Oxide Particles by Hydrogen Studied in an Environmental TEM. *J. Mater. Sci.* **2013**, *48*, 2893–2907. [CrossRef]
25. Grosvenor, A.P.; Biesinger, M.C.; Smart, R.S.C.; McIntyre, N.S. New Interpretations of XPS Spectra of Nickel Metal and Oxides. *Surf. Sci.* **2006**, *600*, 1771–1779. [CrossRef]
26. Karslıoğlu, O.; Trotochaud, L.; Zegkinoglou, I.; Bluhm, H. X-Ray Spectroscopic Characterization of BaO, $Ba(OH)_2$, $BaCO_3$, and $Ba(NO_3)_2$. *J. Electron. Spectrosc. Relat. Phenom.* **2018**, *225*, 55–61. [CrossRef]
27. Trzcinski, M.; Balcerowska-Czerniak, G.; Bukaluk, A. XPS Studies of the Initial Oxidation of Polycrystalline Rh Surface. *Catalysts* **2020**, *10*, 617. [CrossRef]
28. Cortés-Reyes, M.; Azaoum, I.; Molina-Ramírez, S.; Herrera, C.; Larrubia, M.Á.; Alemany, L.J. NiGa Unsupported Catalyst for CO_2 Hydrogenation at Atmospheric Pressure. Tentative Reaction Pathways. *Ind. Eng. Chem. Res.* **2021**, *60*, 18891–18899. [CrossRef]
29. Loy, A.C.M.; Ng, W.L.; Ma, J.; Uddin, M.H.; Vongsvivut, J.; Tobin, M.J.; Samudrala, S.P.; Bhattacharya, S. Deciphering the Role of Cu^0 and $Cu^{\sigma+}$ in Engendering the Hydrogen Production from Glycerol Reforming over Cu/CeO_2: The Effect of Different Cu Precursors. *Appl. Catal. B Environ. Energy* **2025**, *365*, 124865. [CrossRef]
30. Idriss, H.; Llorca, J. Low Temperature Infrared Study of Carbon Monoxide Adsorption on Rh/CeO_2. *Catalysts* **2019**, *9*, 598. [CrossRef]
31. Hadjiivanov, K.; Ivanova, E.; Knözinger, H. FTIR Study of Low-Temperature CO Adsorption on Y Zeolite Exchanged with Be^{2+}, Mg^{2+}, Ca^{2+}, Sr^{2+} and Ba^{2+} Cations. *Microporous Mesoporous Mater.* **2003**, *58*, 225–236. [CrossRef]

Disclaimer/Publisher's Note: The statements, opinions and data contained in all publications are solely those of the individual author(s) and contributor(s) and not of MDPI and/or the editor(s). MDPI and/or the editor(s) disclaim responsibility for any injury to people or property resulting from any ideas, methods, instructions or products referred to in the content.